Remote Sensing of Environment 204 (2018) 472–484

Contents lists available at ScienceDirect

Remote Sensing of Environment

journal homepage: www.elsevier.com/locate/rse

Propagation of uncertainty in atmospheric parameters to hyperspectral unmixing

Nitin Bhatia[a,b,*], Marian-Daniel Iordache[a], Alfred Stein[b], Ils Reusen[a], Valentyn A. Tolpekin[b]

[a] Remote Sensing Unit, Flemish Institute for Technological Research, Mol 2400, Belgium
[b] Department of Earth Observation Science, Faculty of Geo-Information Science and Earth Observation, University of Twente, Netherlands

ARTICLE INFO

Keywords:
Atmospheric correction
Uncertainty propagation
Column water vapor
Aerosol optical depth
Adjacency range
Hyperspectral unimixing

ABSTRACT

Atmospheric correction (AC) is important in pre-processing of airborne hyperspectral imagery. AC requires knowledge on the atmospheric state expressed by atmospheric condition parameters. Their values are affected by uncertainties that propagate to the application level. This study investigates the propagation of uncertainty from column water vapor (CWV) and aerosol optical depth (AOD) towards abundance maps obtained by means of spectral unmixing. Both Fully Constrained Least Squares (FCLS) and FCLS with Total Variation (FCLS-TV) are applied. We use five simulated datasets contaminated by various noise levels. Three datasets cover two spectral scenarios with different endmembers. A univariate and a bivariate analysis are carried out on CWV and AOD. The other two datasets are used to analyze the effect of surface albedo. The analysis identifies trends in performance degradation caused by the gradual shift in parameter values from their true value. The maximum achievable performance depends upon spectral characteristics of the datasets, noise level, and surface albedo. As expected, under noisy conditions FCLS-TV performs better than FCLS. Our research opens new perspectives for applications where estimation of reflectance is so far considered to be deterministic.

1. Introduction

Hyperspectral imaging sensors record the at sensor radiance reflected from a surface, for hundreds of narrow contiguous spectral bands. A recorded image can thus be seen as a three dimensional cube with two spatial dimensions and one spectral dimension. A pixel in such a cube usually covers an area comprising several endmembers. These mixed pixels are in contrast with pure pixels that cover a single endmember. The occurrence of mixed pixels is due to two main reasons: i) the spatial resolution of a hyperspectral sensor is relatively low, thus, several endmembers share the spatial extent of a pixel, and ii) the underlying surface is a mixture of several materials.

As important information about the scene might reside in mixed pixels, extraction of quantities of interest at the subpixel level is needed. Spectral unmixing is a popular extraction method at the subpixel level. It exploits spectral information to derive the endmembers in the scene, their spectral signatures, and their fractional abundances, i.e. areas occupied by each endmember in each pixel. For a comprehensive review of unmixing techniques, see Bioucas-Dias et al. (2012) and the references therein. In this study, we rely on the Linear Mixture Model (LMM) (Keshava, 2003). It expresses the observed spectrum of a pixel as a linear combination of the spectra of the endmembers weighted by their fractional abundances.

Spectral unmixing using the recorded radiance is challenging in the presence of the Earth atmosphere. This is primarily because of the interaction of the surface reflected radiation with the atmospheric constituents while propagating along the path from the target surface to the sensor (Verhoef and Bach, 2003). The interaction generates two main atmospheric effects: absorption by atmospheric gases in particular water vapor and ozone and aerosols in the visible and near-infrared spectral range and scattering by aerosols and molecules (Lenoble, 1998). In addition, on the path of the beam to the sensor, reflection by the surrounding area of the target pixel and radiance backscattered by the atmosphere that did not interact with the surface distorts the at sensor radiance.

An Atmospheric Correction (AC) algorithm retrieves the surface reflectance from the at sensor radiance. AC algorithms can be divided into scene based empirical algorithms and algorithms based on radiative transfer modeling. We use the latter, as it is a mature approach for routine processing of hyperspectral image data (Gao et al., 2006).

In radiative transfer modeling, the target radiance can be derived assuming a plane-parallel geometry of the atmosphere, whereas the viewing and illumination geometry and total optical depth of the atmosphere are known. For a reliable estimate of reflectance, the

* Corresponding author.
E-mail address: nitin.bhatia@vito.be (N. Bhatia).

http://dx.doi.org/10.1016/j.rse.2017.10.008
Received 25 September 2016; Received in revised form 28 September 2017; Accepted 9 October 2017
Available online 27 October 2017

concentration of the atmospheric scatters and absorbers, i.e. the optical parameters, should be available at the time of imaging. In this paper, we analyze the effect of uncertainty in estimations of atmospheric aerosol optical depth (AOD) and column water vapor (CWV). Both CWV and AOD are highly varying in space and time. Thus, they are estimated directly from satellite or airborne (remote) observations. With knowledge of CWV and AOD, transmission of radiation through the atmosphere can be simulated.

Estimation of CWV from at sensor radiance consists of identification of the measurement channels, identification of reference channels, and using a relation between reference and measurement channels (Carrere and Conel, 1993). These methods are limited with respect to several assumptions. First, surface reflectance is assumed to vary with wavelength in a linear way; second, the effect of sensor noise is often not considered, and third, uncertainty emerging from instrument characterization is ignored (Rodger, 2011; Qu et al., 2003).

Estimation of AOD consists of determining aerosol radiative properties characterized by their shape, their size, their chemical composition, and total amount (Diner et al., 2005). The MODIS science team (Remer et al., 2005) has developed the dense dark object method to estimate AOD that is further developed in Richter et al. (2006). The limitation of such methods is their suitability for pixels with dense vegetation. For scenes with dark pixels that are clustered at a few locations, pixelwise estimation of AOD is challenging. Besides, at sensor based inference of AOD is adversely affected by noise of at sensor radiance.

These assumptions and limitations, reasonable as they are, cause uncertainty in the estimation of CWV and AOD which likely propagates to reflectance estimates.

The objective of this paper is to analyze the impact of uncertainty in unmixing caused by CWV and AOD, given their specific influence on the estimated reflectance spectra. A basic hypothesis of unmixing is that the estimated reflectance spectra are free from atmospheric artefacts. By ignoring uncertainty in the AC parameters, however, it is likely that this hypothesis is violated. The paper specifically focuses on an operational processing chain. The operational processing chain is implemented in the multi-mission Processing, Archiving, and distribution Facility (PAF) for Earth observation products (Richter, 2007). Experiments in this paper are performed using the PAF incorporated in the Central Data Processing Center (CDPC) (Biesemans et al., 2007) at the Flemish Institute for Technological Research.

2. Theoretical background

2.1. Basic atmospheric effect modeling

The fraction (ρ_t) of the total irradiance at the surface (E_g) reflected by the earth surface depends upon the type of surface, illumination (θ_s), viewing geometry (θ_v), and wavelength (λ). On the path of the beam to the sensor other radiation components are added to the radiance reflected by the surface ($L_t(\lambda)$) due to atmospheric scattering. We distinguish four contributions to the at sensor radiance ($L_{rs,t}(\lambda)$):

$$L_{rs,t}(\lambda) = L_t(\lambda) + L_{pa}(\lambda) + L_{pb}(\lambda) + L_b(\lambda). \quad (1)$$

$L_t(\lambda)$ contains the target surface information, $L_{pa}(\lambda)$ and $L_{pb}(\lambda)$ are path radiance and background path radiance, respectively, that enter the IFOV of the sensor due to scattering, and $L_b(\lambda)$ is the background radiance, or adjacency effect, being the average radiance of the surrounding surface.

For a target surface with reflectance $\rho_t(\lambda)$ and background reflectance $\rho_{bck}(\lambda)$, the background path radiance, background radiance, and target radiance are:

$$L_{pb}(\lambda) = \frac{1}{\pi}\rho_{bck}(\lambda)T^{+}_{tot}(\tau, \theta_v, \lambda)E_g(\lambda), \quad (2)$$

$$L_b(\lambda) = \frac{1}{\pi}\rho_{bck}(\lambda)T^{+}_{dir}(\tau, \theta_v, \lambda)E_g(\lambda), \quad (3)$$

$$L_t(\lambda) = \frac{1}{\pi}\rho_t(\lambda)T^{+}_{dir}(\tau, \theta_v, \lambda)E_g(\lambda), \quad (4)$$

where T^{+}_{tot} expresses the total upward transmittance, which is further subdivided in direct transmittance (T^{+}_{dir}) and diffuse transmittance (Haan and Kokke, 1996). Let the residual terms in Eq. (1) be denoted by:

$$L_{rs,b}(\lambda) = L_{pa}(\lambda) + L_{pb}(\lambda) + L_b(\lambda). \quad (5)$$

Then the background reflectance can be retrieved using

$$\rho_{bck}\ (\lambda) = \frac{L_{rs,b}(\lambda) - L_{pa}(\lambda)}{C} \quad (6)$$

with

$$C = \cos(\theta_s)T^{+}_{tot}(\tau, \theta_v, \lambda)T^{-}_{tot}(\theta_s, \lambda)F + S[L_{rs,b}(\lambda) - L_{pa}(\lambda)]$$

where S is the spherical albedo for illumination from below of the atmosphere and T^{-}_{tot} expresses the total downward transmittance. Substituting the expression for $\rho_{bck}(\lambda)$, the target reflectance equals

$$\rho_t(\lambda) = \frac{L_{rs,t}(\lambda) - L_{pa}(\lambda) + [L_{rs,t}(\lambda) - L_{rs,b}(\lambda)]T^{+}_{dir}(\tau, \theta_v, \lambda)T^{+}_{diff}(\tau, \theta_v, \lambda)}{C}. \quad (7)$$

The basic atmospheric effect model is well described in Gao et al. (2009). We use MODTRAN 4 (Berk et al., 2000) to estimate the radiance components in Eq. (7). It computes absorption and scattering in the terrestrial atmosphere at high spectral resolution and is treated below as a black box. It allows one to pixelwise solving the DIScrete Ordinate Radiative Transfer (DISORT) (Stamnes et al., 1988) for accurate computations of atmospheric multiple scattering. In an operational processing chain, however, the considerable execution time to do so is a problem. Therefore, MODTRAN 4 is executed for a uniform Lambertian surface reflectance with a spectrally flat surface albedo of $A_{pp} = 0$, $A_{pp} = 0.5$, and $A_{pp} = 1.0$. In this way, the various radiance components for a given atmospheric state and angular geometry are determined. This is the MODTRAN interrogation technique that has been used in operational processing chains to derive the same radiance component as in Eq. (7) (Verhoef and Bach, 2003; Sterckx et al., 2016). MODTRAN 4 provides four radiance components:

1. The total radiance as measured by the sensor, $L_{rs,t}(\lambda)$,
2. The total path radiance $L_{path}(\lambda)$ that consists of the light scattered in the path,
3. The total ground radiance that consists of all the light reflected by the surface and traveling directly towards the sensor, $L_{gnd}(\lambda)$,
4. The direct ground reflectance, $L_{dir}(\lambda)$ as a fraction of $L_{gnd}(\lambda)$ resulting from direct illumination of the ground surface.

The four components are then combined using Eq. (7).

2.2. The linear mixture model (LMM) and unmixing methods

Let $y \in \mathbb{R}^B$ be the reflectance spectrum of one pixel, where B is the number of spectral bands. According to the LMM, it can be expressed as a linear combination of the spectra of the endmembers, weighted by their fractional abundances:

$$y = A \cdot x + n. \quad (8)$$

Here, $A \in \mathbb{R}^{B \times m}$ is the set of endmembers in the scene serving as a spectral library containing m pure spectra, $x \in \mathbb{R}^m$ is the vector of corresponding fractional abundances compatible with A, and $n \in \mathbb{R}^B$ is a noise vector. In this paper, we assume that A is available a priori. Unmixing thus aims at identifying the atoms of A which are active in each pixel and their respective abundances. To solve Eq. (8), we

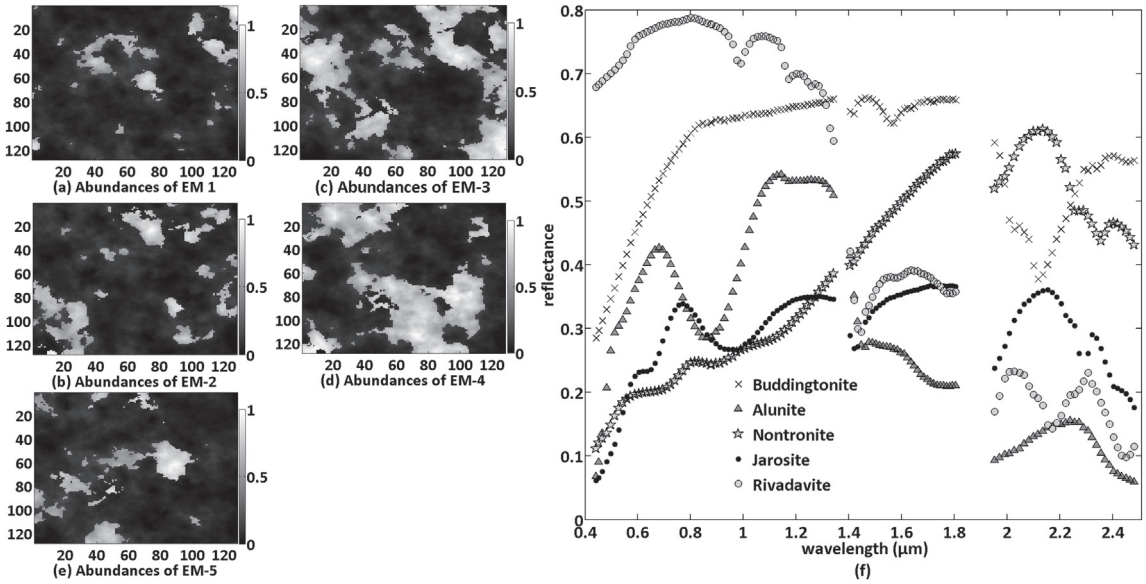

Fig. 1. Fractional abundances of the five (spectrally distinct) endmembers (a)–(e) and their corresponding spectral signatures (f) generating the first geological dataset.

consider the classical least-squares solution obtained by solving:

$$\min_{x} \frac{1}{2} \|A \cdot x - y\|_2^2. \tag{9}$$

Two constraints, arising from the physical meaning of the fractional abundances, can be imposed on Eq. (9): 1) the non-negativity constraint (ANC), and 2) the sum-to-one constraint (ASC) (Heinz and Chang, 2001).

In addition, we take intrinsic spatial smoothness into account as an important characteristic of natural scenes. We use the Sparse Unmixing via Variable Splitting, Augmented Lagrangian and Total Variation (SUnSAL-TV) (Iordache et al., 2012) to obtain a solution with piecewise smooth transitions of the abundance fractions in neighboring pixels. SUnSAL-TV solves the optimization problem:

$$\min_{X} \frac{1}{2} \|AX - Y\|_F^2 + \lambda_1 \|X\|_{1,1} + \lambda_{TV} \mathrm{TV}(X), \tag{10}$$

where

$$\mathrm{TV}(X) \equiv \sum_{\{i,j\} \in \varepsilon} \|x_i - x_j\|_1 \tag{11}$$

is a vector extension of the non-isotropic TV (Chambolle, 2004) and ε denotes the set of neighbors in the image. In Eq. (10), $Y \in \mathbb{R}^{L \times n}$ is the observed data matrix with each column containing the observed spectrum at a pixel, $X \in \mathbb{R}^{m \times n}$ is the matrix of fractional abundances, $\|X\|_F \equiv \sqrt{\mathrm{trace}\{XX^T\}}$ represents the Frobenius norm of X and $\|X\|_{1,1} \equiv \sum_{i=1}^{n} \|\mathbf{x}_i\|_1$, with x_i denoting the i^{th} column of X. The first term in Eq. (10) measures the data misfit, the second term forces the matrix of fractional abundances to be sparse, and the last term accounts for spatial homogeneity of the abundance maps. The parameters $\lambda_1 \geq 0$ and $\lambda_{TV} \geq 0$ are regularization parameters. SUnSAL-TV introduces a set of new variables per regularizer and then uses the Alternating Direction Method of Multipliers (ADMM) (Jonathan and Bertsekas, 1992) to solve the resulting constrained optimization problem. In our experiments, we neglect sparsity as the spectral libraries employed will contain a small number of endmembers. We use SUnSAL-TV applying both ANC and ASC to solve both optimization problems Eqs. (9) and (10), as follows:

- Fully constrained least squares (FCLS): no sparsity is enforced and no spatial information is considered. This situation is encountered if the regularization parameters $\lambda_1 = 0$ and $\lambda_{TV} = 0$;
- FCLS with Total Variation (FCLS-TV): Only spatial information is considered in SUnSAL-TV by setting $\lambda_1 = 0$ and $\lambda_{TV} > 0$.

The ASC, often ignored due to signature variability (Bateson et al., 2000), is used in this work as we assumed the set of image endmembers to be known and hence no sparsity is enforced on the vectors of fractional abundances.

3. Datasets

Three synthetic datasets are used to quantify the uncertainty propagated at two levels: reflectance cubes as a level2 product and abundance maps as a level3 product. These two products are estimated under various atmospheric conditions: i) low to moderate to high scattering conditions; ii) low to moderate to high absorption conditions; iii) the usual conditions, related to the moderate atmospheric conditions under which most of the airborne campaigns are performed.

We create two datasets for a geological scenario and one dataset for a scenario containing vegetation. Further, we use two Spectral Scenarios (SS): SSa with spectrally distinct endmembers in a scene; SSb with spectrally similar endmembers in a scene. The two spectral scenarios are linked to the three synthetic datasets.

3.1. The synthetic datasets

The two geological datasets are generated using the MATLAB Hyperspectral Imagery Synthesis tools, available online (Matlab-Toolbox, 2012). They contain two distinct sets of five endmembers, collected from the USGS spectral library (Kokaly et al., 2017). We use the following spectrally distinct endmembers to generate the first geological dataset: Buddingtonite, Alunite, Montmorillonite, Jarosite, and Rivadavite (Fig. 1). The spectrally similar endmembers, used to generate the second geological dataset, are signatures of a single mineral, Nontronite, to address endmember variability (Fig. 2). All endmember spectra were resampled to the central wavelengths of the HyMap airborne hyperspectral sensor (Cocks et al., 1998). Each dataset contains 128×128 pixels on 126 spectral bands with the spatial resolution of 2.5 m along track and 2.0 m across track.

The vegetation dataset is generated following (Iordache et al., 2012) and is a hyperspectral image cube of 75×75 with 126 spectral bands. There are five endmembers present in the scene: leather oak, dry grass, sandy loam, construction concrete, and asphalt. These endmembers were obtained as follows: dry grass and leather oak spectra from the database of Jasper Ridge, spectral library (ENVI-Team, 2014) and construction, sandy loam, and asphalt from the database of the Johns

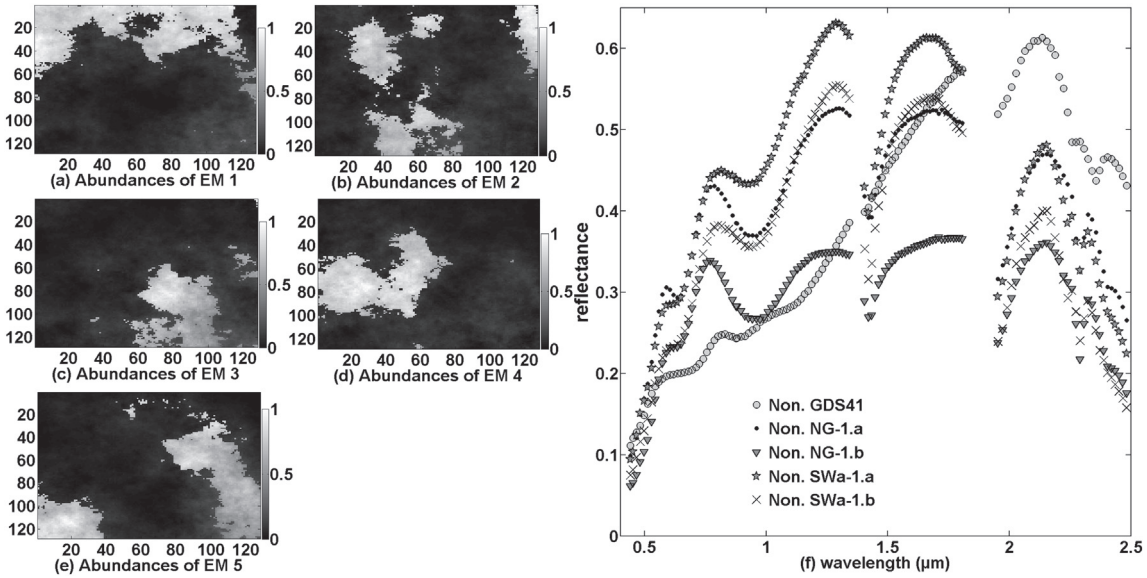

Fig. 2. Fractional abundances of the five (spectrally similar) Nontronite (Non.) types (a)–(e) and their corresponding spectral signatures (f) generating the second geological dataset.

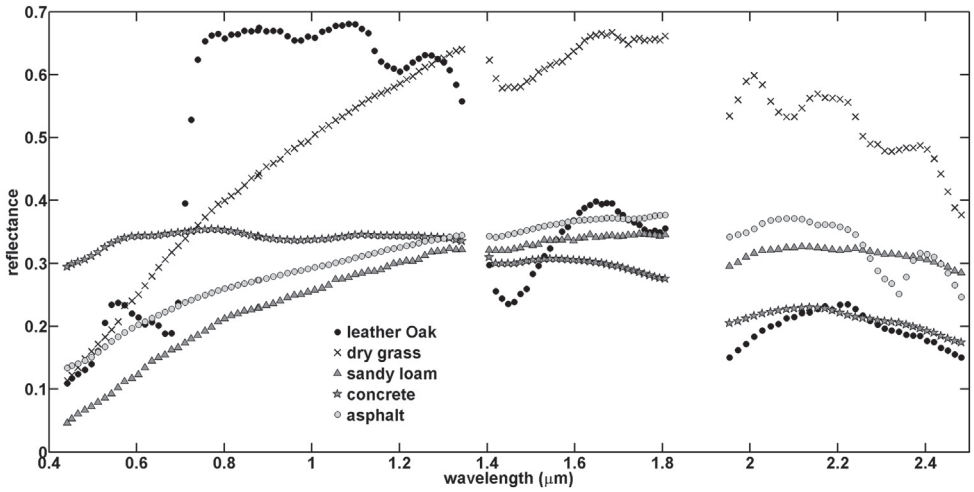

Fig. 3. Spectral signatures of the five materials used to generate the vegetation dataset.

Hopkins University Spectral Library (Baldridge et al., 2009). All endmember spectra were resampled to the central wavelengths of the HyMap airborne hyperspectral sensor (Fig. 3). The vegetation dataset contains square regions of 5×5 pixels, which are spectrally homogeneous, and all pixels within a square region have the same reflectance values. Fig. 4 depicts spatial arrangement of the homogenous regions and ground truth fractional abundance maps.

All datasets are generated according to the LMM, including the ANC and ASC.

3.2. Case study: variability of surface albedo (dark and bright surfaces)

The surface albedo influences the quality of the spectra retrieved via atmospheric correction (AC), independently from the effects of the uncertainty in the AC parameters. Aerosol optical depth is particularly important in this respect, as it influences the amplitude of the spectra in a large range of wavelengths. This case study analyzes the effect of surface albedo on reflectance and abundance estimates with two datacubes comprising dark and bright targets separately. The bright target datacube is generated using spectra of five minerals: Albite, Ammonio-Illite, Ammonio-Alunite, Muscovite, and Topaz. The dark surface is generated mainly using man-made materials: Black tar paper, Cinders, Construction asphalt, Reddish asphalt, and Bornoite (mineral). Each dataset contains 128×128 pixels with 126 spectral bands and the spatial resolution of 2.5 m along track and 2.0 m across track. The spectra of these materials are presented in Fig. 5.

3.3. Addition of noise to the simulated datasets

Sensor noise and processing noise are major sources of distortion. Sensor noise refers to the random electronic noise like dark current, processing noise occurs due to the final pre-processing steps on the reflectance datacube, e.g. spectral smoothing. We added the two types of noise to the datasets at two stages: sensor noise to the radiance cube and processing noise to the estimated reflectance cube. In order to observe the effect of the different noise levels we considered three levels of the correlated processing noise, with signal-to-noise ratios (SNR): 30, 40, and 50 dB, respectively. All correlated noise levels were generated from independent, normally distributed noise by low-pass filtering with a normalized cut-off frequency of $\frac{8 \cdot \pi}{B}$ for each SNR.

Fig. 6 shows four estimates of band 100 (2.2 μm) of the reflectance cube when random (white) sensor noise with SNR: 30, 40, 50, and 60 dB is added to the at sensor radiance. True AC parameters were employed and no correlated noise was added to the reflectance cube. From visual interpretation we conclude that sensor noise with SNR = 60 dB is a realistic choice as the other noise levels severely

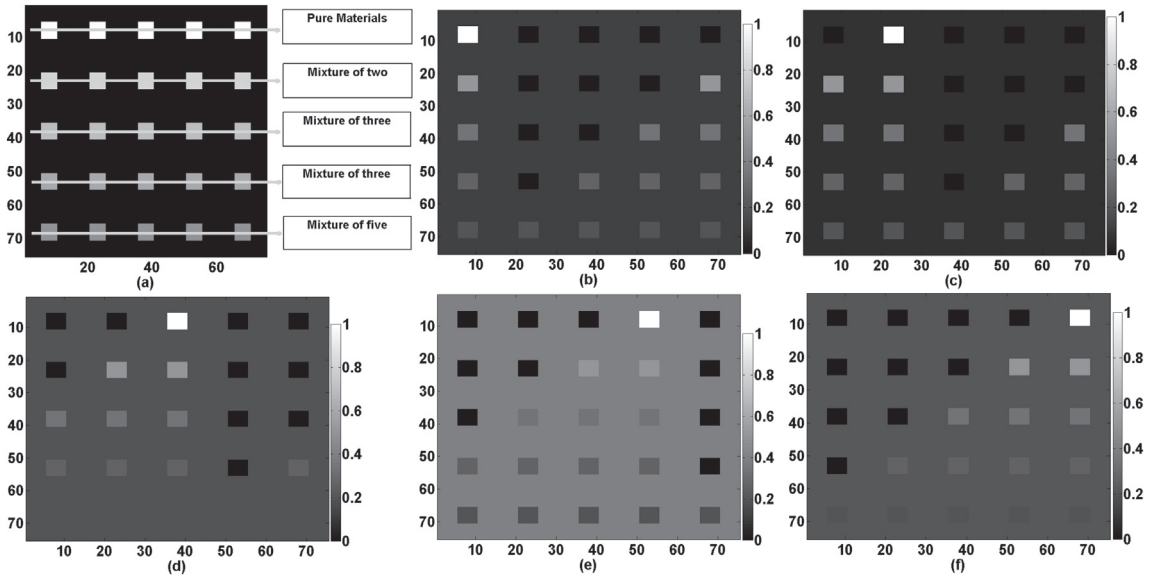

Fig. 4. Spatial arrangement of the homogenous regions (a) and ground truth fractional abundance maps (b)–(f). The square regions at the top are pure and correspond to the five endmembers. The other square regions are mixed with the number of endmembers ranging between two and five. The remaining pixels (image background) contain a mixture of the five endmembers in which the abundance fractions were randomly fixed to 0.513, 0.1476, 0.1158, 0.1242 and 0.0994, respectively.

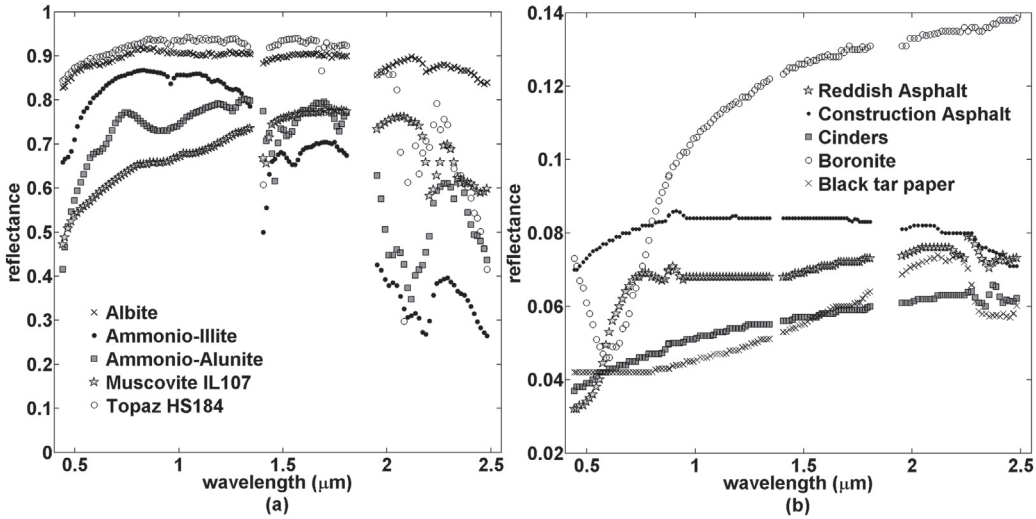

Fig. 5. Spectra of the materials used to generate the bright surface in (a) and spectra of the materials used to generate the dark target surface in (b).

distort the images when other errors are missing.

4. Experiments

Atmospheric correction, as a mathematical model of an atmosphere, returns an estimate of reflectance for any physically realizable values of column water vapor, aerosol optical depth and other parameters. In our experiments, the other parameters are treated as constants. Column water vapor and aerosol optical depth, however, should also have unique values during atmospheric correction. In simulations, it may be necessary to vary them over a range of values, where the distribution of values reflects the uncertainties of the parameters. We use one-at-a-time variation in aerosol optical depth and column water vapor, i.e. univariate analysis, and their joint variation in a bivariate analysis for the uncertainty analysis. A bivariate analysis permits large deviations from the nominal parameter values, thus allowing evaluation of atmospheric correction for various combinations of column water vapor and aerosol optical depth. We use uniform probability distributions for the two atmospheric parameters, resulting in equally probable samples.

4.1. The forward modeling

At sensor radiance cubes are simulated using the forward radiative transfer modeling using MODTRAN 4. Standard MODTRAN 4 mid-latitude summer model with the rural aerosol model is used and the sensor altitude is approximately 3 km above sea level. In an operational processing chain, realistic aerosol optical depth values that coincide with image acquisition are unavailable (Wilson et al., 2015). As an alternative, image based methods measuring visibility are often used to set aerosol optical profiles (Richter, 2007; Schlapfer, 1998). Here, we specify aerosol optical depth values and their corresponding visibility values so that it is useful to the remote sensing communities dealing with both quantities.

In MODTRAN 4, visibility scales the aerosol content in the atmosphere, whereas AOD specifies extinction due to aerosols at wavelength λ and is the product of the extinction coefficient $EXT(\lambda)$ and the path length. Aerosol optical depth asymptotically decreases with increasing visibility. At 550 nm the contributions of molecular depth, ozone depth, and trace gases usually are small and aerosol optical depth is the main contributor to the total optical depth of the atmosphere i.e. $EXT(550)$ is

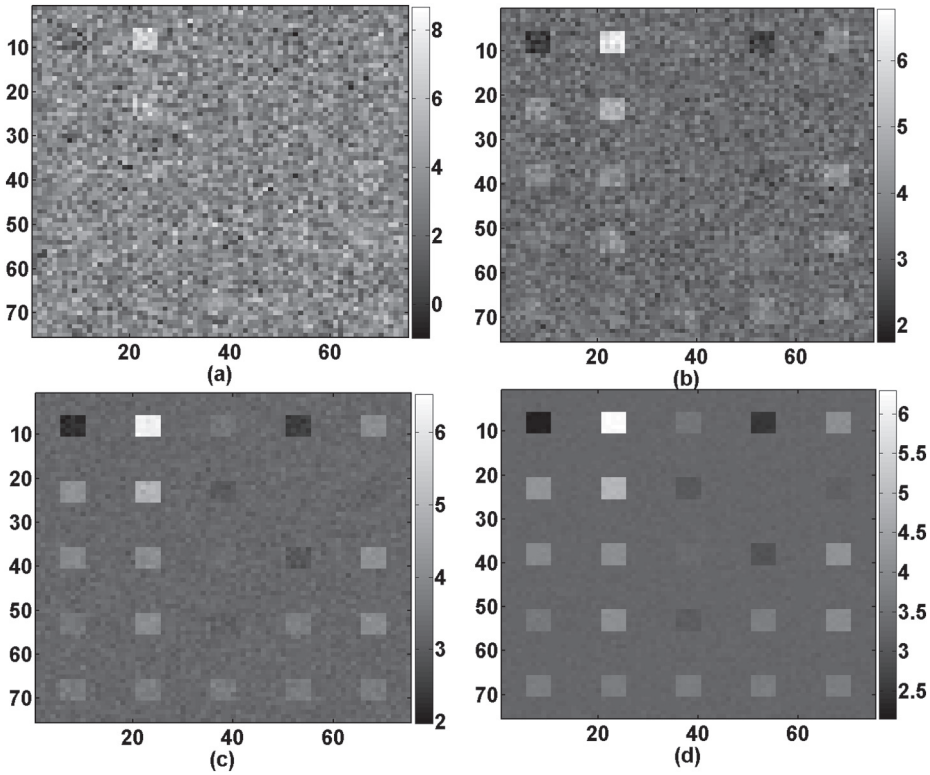

Fig. 6. Band at (2.2 μm) of the estimated reflectance with 30 dB (a), 40 dB (b), 50 dB (c), and 60 dB (d) noise levels. The noise levels strongly distort the reflectance image.

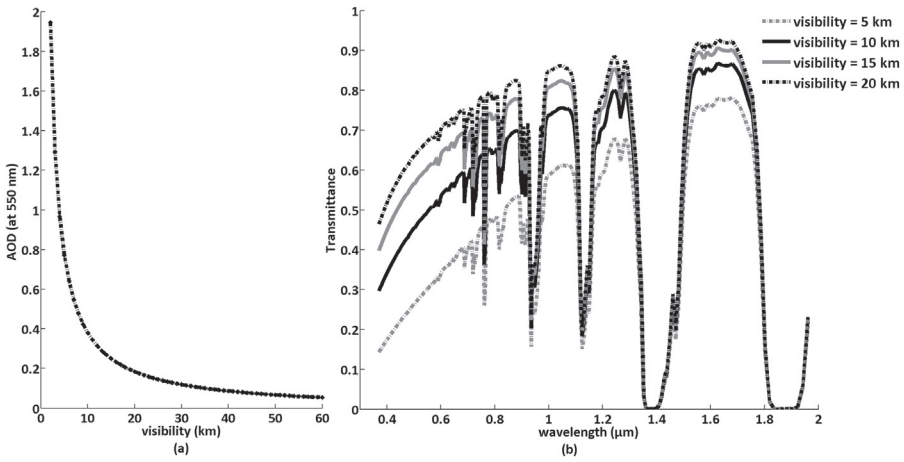

Fig. 7. Relation between visibility and aerosol optical depth in (a) and effect of visibility on atmospheric transmittance in (b). Standard MODTRAN 4 mid-latitude summer model with the rural aerosol model is used while sensor altitude is approximately 3 km and column water vapor equals 2.0 g·cm^{-2} and other MODTRAN parameters are at their default values.

directly related to aerosol optical depth. A high precision in aerosol optical depth can be achieved by subtracting the Rayleigh scattering coefficient and a very small trace gas depth from a known total optical depth. In MODTRAN 4, for $\lambda = 550$ nm and for a geographic region at mid-latitude during the summer season, visibility is related to aerosol optical depth (Fig. 7) as,

$$\text{visibility} = \frac{\ln(50)}{EXT(550) + 0.01159}, \tag{12}$$

where, 0.01159 km^{-1} is the surface Rayleigh scattering coefficient for $\lambda = 550$ nm. Therefore, visibility is given as a parameter for transmittance simulations for a given illumination and viewing geometry. This leads to a look-up table of visibility against transmittance. The relation between visibility and aerosol optical depth, jointly with the effect of visibility on atmospheric transmittance, are illustrated in Fig. 7.

In univariate and bivariate analysis applied to the FCLS-TV algorithm, the regularization parameter λ_{TV} is set to values between 0 and 0.06 with a step size of 0.01, and the best performance among all values is retained. Average performances over ten runs are taken.

4.2. Experimental setup for univariate analysis

The univariate analysis experiments for aerosol optical depth consist of three ranges: high to moderate (visibility: 4–26 km), moderate to low (visibility: 16–45 km), and low (visibility: 45–72 km). From our experience with real images processed in the CDPC, we observed that the reflectance is not sensitive to visibility values above 60 km. Thus, the maximum value of visibility is set to 72 km. Each visibility range is associated with an experiment given in Table 1, where column water vapor is kept fixed to the value used in the forward modeling. Likewise, the experiments for column water vapor consist of two column water vapor ranges: low to moderate (0.1–1.0 g·cm^{-2}) and moderate to high (1.0–2.25 g·cm^{-2}). Each column water vapor range is associated with an experiment given in Table 2. In these experiments, visibility is kept fixed to the value used in the forward modeling. We used the same atmospheric settings to analyze the propagation of uncertainty to the

Table 1
Visibility (km) and corresponding aerosol optical depth ranges to generate various atmospheric combination to perform univariate analysis of aerosol optical depth for geological scenario datasets with distinct and similar endmembers, respectively. The sampling rate is 2 km and column water vapor is fixed at 1.5 g·cm^{-2}.

Scattering condition	Aerosol optical depth range	True aerosol optical depth	Visibility range	True visibility
High to moderate	1.42–0.28	0.47	4–26	15
Moderate to low	0.45–0.18	0.28	16–45	28
Low	0.18–0.11	0.14	45–72	60

Table 2
Column water vapor ranges (g·cm^{-2}) to generate various atmospheric combination to perform univariate analysis of column water vapor for the geological datasets with distinct and similar endmembers. The sampling rate is 0.05 g·cm^{-2} and the visibility is fixed at 15 km (i.e. aerosol optical depth equals 0.48).

Absorption condition	Column water vapor range	True column water vapor
Low to moderate	0.1–1.0	0.5
Moderate to high	1.0–2.25	1.5

abundance maps. The unmixing performed using the FCLS and FCLS-TV is repeated for noiseless data and correlated noise with SNR of 50 dB, 40 dB and 30 dB.

4.3. A univariate analysis of dark and bright targets

This experiment analyzes the joint influence of aerosol optical depth uncertainty and albedo amplitude on the spectral quality of the estimated reflectance cube and on the fractional abundances derived from it.

For the forward modeling of dark and bright target surfaces, low scattering (aerosol optical depth = 0.14) and high scattering (aerosol optical depth = 0.48) are considered, whereas column water vapor is fixed to 1.5 g·cm^{-2}, resulting in four at sensor radiance cubes. AC is evaluated for two discrete sets of samples of the aerosol optical depth in the ranges (1.42–0.28) and (0.16–0.13), corresponding to visibility ranges 6–27 km and 51–69 km, respectively.

4.4. Experimental setup for a bivariate analysis

The bivariate analysis applied to the vegetation dataset analyzes the joint effect of column water vapor and aerosol optical depth on atmospheric correction. Column water vapor and visibility are varied within the ranges 1.35–1.65 g·cm^{-2} and 15–45 km, corresponding to aerosol optical depth values between 0.48 and 0.18, with reference column water vapor and visibility set to 1.5 g·cm^{-2} and 30 km, respectively. These experiments are repeated for data without correlated noise and for data perturbed by correlated noise with SNR of 50 dB, 40 dB, and 30 dB. This atmospheric setting is also used to analyze the propagation of uncertainty to abundance mapping.

4.5. Uncertainty propagation

To quantitatively assess the propagation of uncertainty we use the signal-to-reconstruction-error SRE$\equiv \frac{E[\|x\|_2^2]}{E[\|x-\hat{x}\|_2^2]}$ for both the estimated reflectance and fractional abundances. Here, x is the reference signal and $\hat{x}$ is an estimation of x. SRE provides more information on the power of the signal w.r.t. the power of the error than, e.g., the Root Mean Squared Error (RMSE) (Iordache et al., 2011). In all experiments, we report SRE measured in dB: SRE(dB) = $10\log_{10}(SRE)$.

In addition, to quantify the pixelwise uncertainty in the estimates of reflectance and abundance maps, we measure two other quantitative errors: Normalized Root Mean Square Error (NRMSE) = $\frac{\text{RMSE}}{\max(x)-\min(x)}$ and Mean Absolute Percentage Error (MAPE) = $\sum_{t=1}^{n}\left|\frac{x_t-\hat{x}_t}{x_t}\right| \times 100$.

5. Experimental results

5.1. Univariate analysis of aerosol optical depth

Fig. 8 shows results of univariate analysis of aerosol optical depth for the geological dataset with distinct endmembers with different degrees of correlated noise added to the dataset. The maximum performance is achieved if visibility is close to the true value. The rate of degradation in performance is higher, shown by the steeper slope, if visibility is underestimated and is smaller if overestimated. This performance trend is valid for all visibility scenarios. The maximum achievable performance varies among the datasets and depends upon the true value of visibility. For the true atmospheric conditions, i.e. the

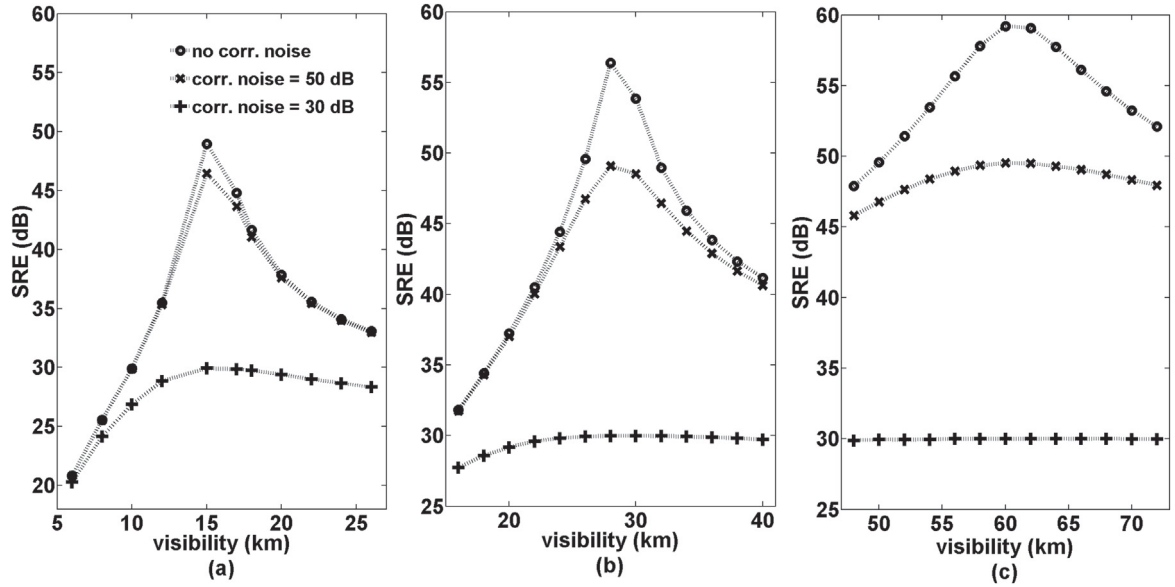

Fig. 8. SRE (dB) values for univariate analysis of aerosol optical depth for the geological dataset with distinct endmembers with and without correlated (corr.) noise, when the true visibility is set to: a) 15 km; b) 28 km, and c) 60 km.

Table 3
Performance ratios for the geological dataset with distinct endmembers ($G_{dist.}$) and the geological dataset with similar endmembers ($G_{sim.}$). P_1 corresponds to noisy data with SNR = 30 dB, while P_2 corresponds to noiseless data. The lower the ratio values, higher the performance degradation during the univariate analysis of the reflectance product.

Label	True visibility (km)	P_1	P_2	Ratio
$G_{dist.}$	15	29.94	48.95	0.612
$G_{sim.}$	15	29.98	56.87	0.527
$G_{dist.}$	28	29.99	56.39	0.532
$G_{sim.}$	28	30	58.88	0.51
$G_{dist.}$	60	30	59.21	0.507
$G_{sim.}$	60	29.98	59.70	0.502

same atmospheric conditions for forward and inverse radiative modeling, the minimum performance is achieved if true visibility equals 15 km, whereas the maximum performance is achieved if true visibility equals 60 km. Ideally, the performances should not vary if atmospheric conditions are kept constant for the forward and inverse radiative modeling. This difference is attributed to surface albedo and is further investigated in Section 5.3.

From Fig. 8, it can be seen that the performance degrades if the data are affected by noise. This observation is valid for all datasets, and the decrease in the performance is stronger if the noise level increases. To quantify this effect, we compute the ratio (R) between the maximum performance for SNR = 30 dB and the maximum performance without correlated noise (Table 3). A low ratio indicates a high degradation. Each noise level limits the maximum achievable performance even at the true value of visibility. This affects the slope between the performance achieved at the true value of visibility and at all other points. For instance, if the true visibility is 15 km and without correlated noise the maximum performance is close to 49 dB and the minimum performance is close to 20 dB, thus the slope is approximately 3.2. With 30 dB correlated noise, the maximum achievable performance is limited to 30 dB and the slope is approximately 1.3. For the two geological scenario datasets, performance of FCLS and FCLS-TV is quantified using reference abundance cubes i.e. ground-truth abundances used to generate those datasets.

Fig. 9 shows the performance of FCLS for noiseless data. Results reveal that for both FCLS and FCLS-TV (not presented), the performance trend is similar to that of reflectance estimates, but its magnitude is lower than the reflectance estimates. The different spectral compositions of the scenes may cause differences in performance between the geological datasets with distinct and similar endmembers. Another explanation may be the difference in surface albedo between the datasets. Further, peak performances are observed at the true value of visibility and at the next higher value of visibility i.e. the performance is insensitive to visibility values between these two points. For the geological dataset with similar endmembers, peak performances are unavailable at the true values and appear at the next lower value of visibility.

Fig. 10 shows the variation of SRE (dB) with respect to λ_{TV} for the geological dataset with distinct endmembers for all scattering scenarios affected by various levels of noise.

For no correlated noise, 50 dB correlated noise and 40 dB correlated noise, the performances of FCLS and FCLS-TV are comparable, whereas FCLS-TV performs better with increasing noise level.

To explore propagation of the uncertainty to the abundance maps, we quantify NRMSE to generate various other results. First, in Fig. 11 a bar graph representing NRMSE of the geological dataset with distinct endmembers is shown. Note, the larger errors are occurring for low visibility values.

Fig. 12 shows propagation of uncertainty in terms of mean NRMSE estimates of endmember-4 abundance maps obtained by varying visibility between 6 and 26 km and their corresponding standard deviation maps. The true visibility is set to 15 km. The mean NRMSE corresponds to a map with the mean values at every pixel computed by an average of NRMSE at each visibility value between 6 and 26 km, with a sampling rate of 1 km.

5.2. Univariate analysis for column water vapor

As for aerosol optical depth, the maximum performance is obtained at the true value of column water vapor. Unlike for aerosol optical depth, however, the performance degradation is sharp and less dependent upon column water vapor overestimation or underestimation. For higher column water vapor ($> 2.0\ g{\cdot}cm^{-2}$) the performance tends to saturate. Further, the maximum attainable performance is independent of the true column water vapor values. This is as expected and different from aerosol optical depth where differences in performance are observed for visibility values of 15 km and 60 km. Performances are higher for geological scenario dataset with similar endmembers. With the increase in noise level, the performance degrades but the peak of the performance remains at the true values i.e. no shift is observed.

For the two geological scenario datasets with distinct and similar endmembers, and for both FCLS and FCLS-TV, the performance trend is similar to that of reflectance estimate, whereas the magnitude of the performances is lower. Unlike aerosol optical depth, no significant variation in performance is observed due to changes in the spectral property i.e. changes of the datasets.

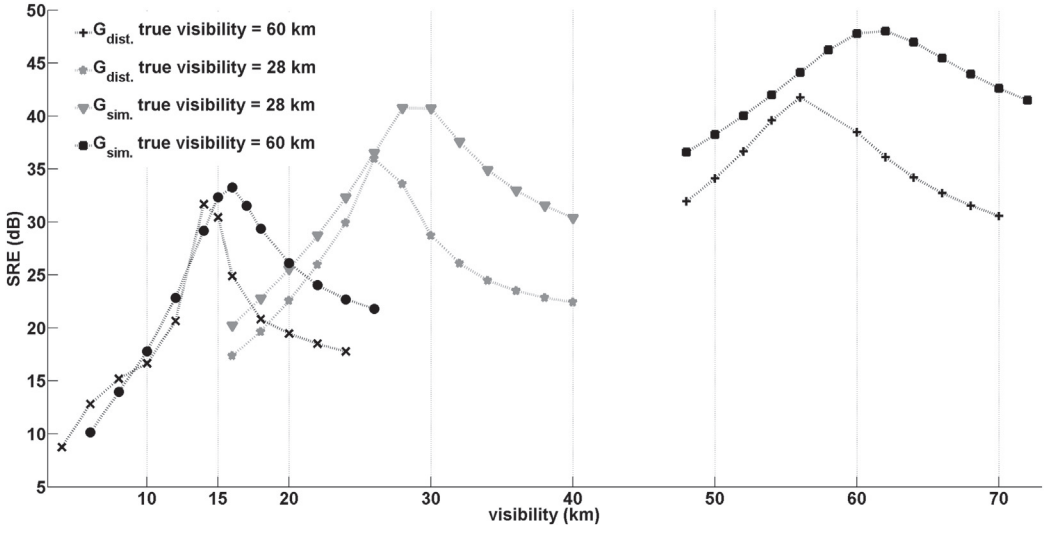

Fig. 9. SRE values for FCLS with the geological dataset with distinct endmembers ($G_{dist.}$) and the geological dataset with similar endmembers ($G_{sim.}$) without correlated noise.

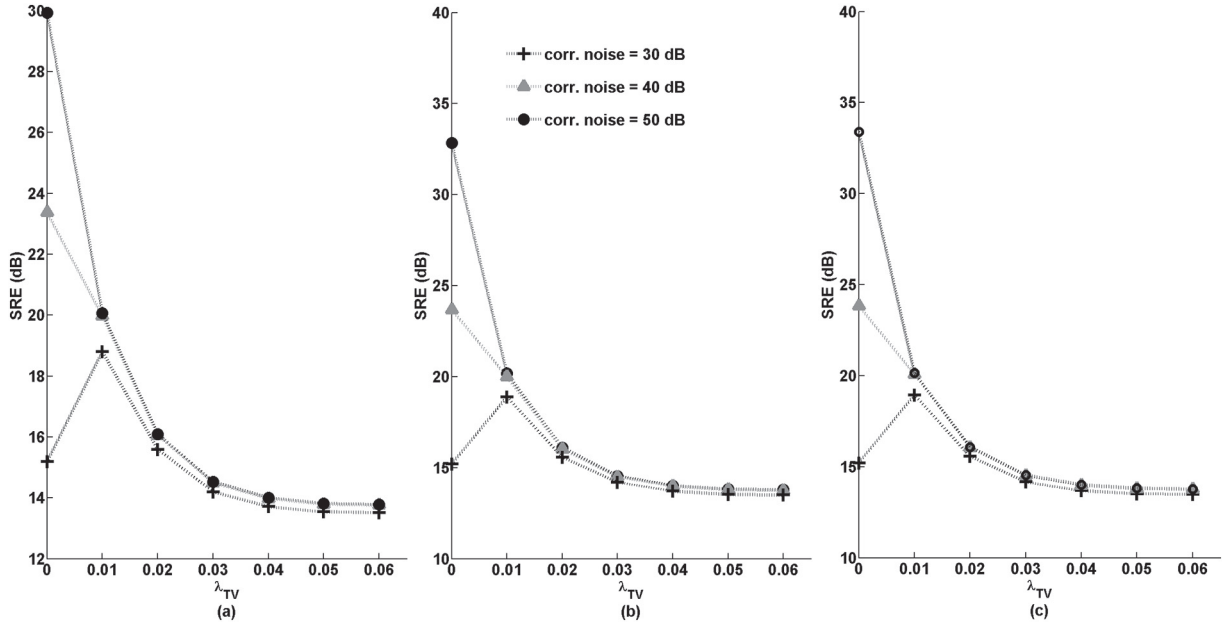

Fig. 10. Variation of SRE(dB) with respect to λ_{TV} values for FCLS-TV in geological dataset with distinct endmembers for the true visibility equals 15 km (a), 28 km (b), and 60 km (c). The optimal value of λ_{TV} corresponds to the maximum value of SRE (dB).

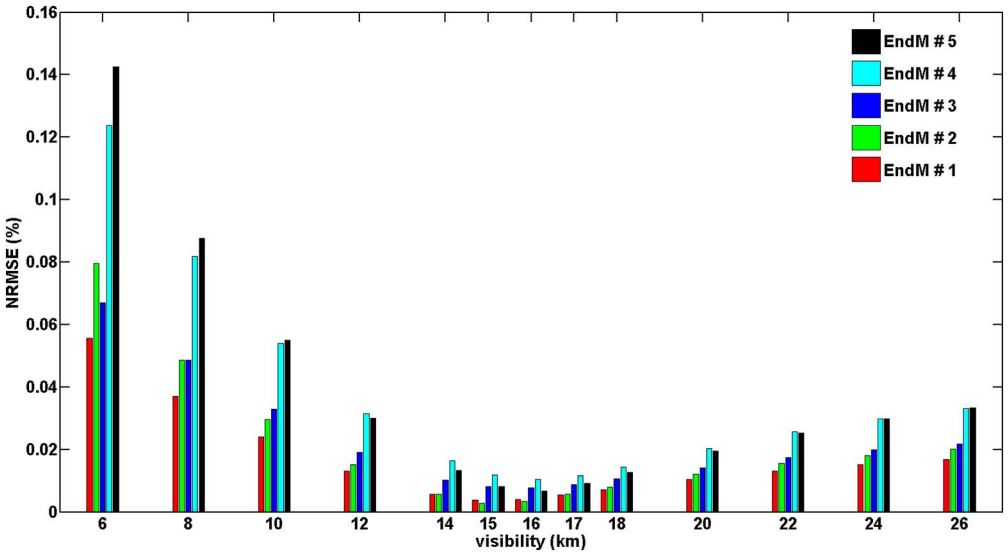

Fig. 11. NRMSE for each endmember of the geological dataset with distinct endmembers for a visibility range 6–26 km when the true visibility is set to 15 km.

Fig. 13 shows a reference spectrum and various spectra of the same material, derived via AC that are distorted due to the uncertainty in visibility and column water vapor. These results illustrate the effect of a parameters' deviation on the spectral quality and depict how deviation in the parameter affect the shape of the spectra, which is an important input for unmixing.

5.3. Univariate analysis of dark and bright targets

Table 4 shows results of the experiment related to the dark and bright targets if no noise is added to the reflectance cubes. For illustration, only performances for the true atmospheric conditions of 15 km and 60 km are shown. At reflectance level, we noted that the performance for the dark targets is lower than the one for the bright targets irrespective of the atmospheric conditions. This trend propagates to the abundance level estimation as well, as shown in Fig. 14. As the unmixing performance follows the trend of the SRE(dB) computed for reflectance, it can be concluded that the abundance maps obtained via unmixing for bright scenes are less affected by uncertainty in the atmospheric correction parameters than those obtained for dark scenes.

5.4. The bivariate analysis for column water vapor and aerosol optical depth

blackThe performance analysis for reflectance and abundance maps is given in Fig. 15. As observed from the univariate analysis experiments, high performance around the true values of column water vapor and visibility is obtained. If the values of the two parameters deviate from the true values, the performance degrades. A general pattern is that the performance tends to saturate, after a relatively low decrease, if visibility is higher than 30 km (overestimation), whereas, if visibility is lower than 30 km (underestimation), the performance sharply declines. For column water vapor, however, performance declines sharply for both overestimation and underestimation.

Fig. 16 shows SRE (dB) of reflectance estimates and abundance estimates under high noise conditions, i.e. 30 dB correlated noise. This

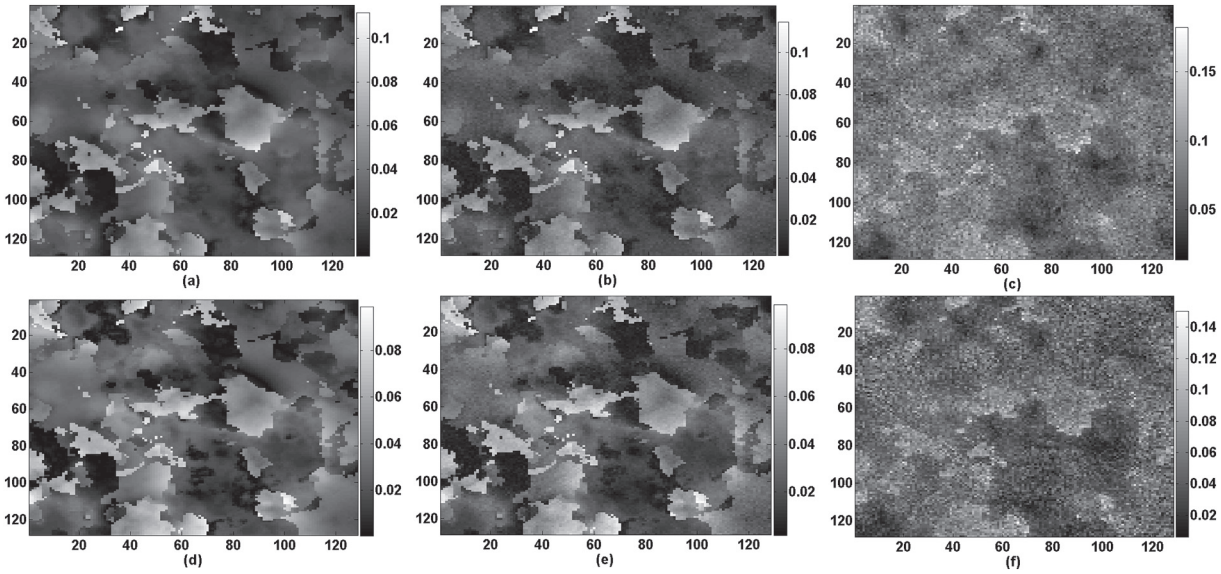

Fig. 12. Mean NRMSE estimates of endmember-4 for no noise (a), 50 dB noise in (b) and 30 dB noise in (c) obtained due to variations in visibility between 6 and 26 km. The corresponding standard deviation are shown in plots (d)–(f) for no noise, 50 dB, and 30 dB noise levels, respectively.

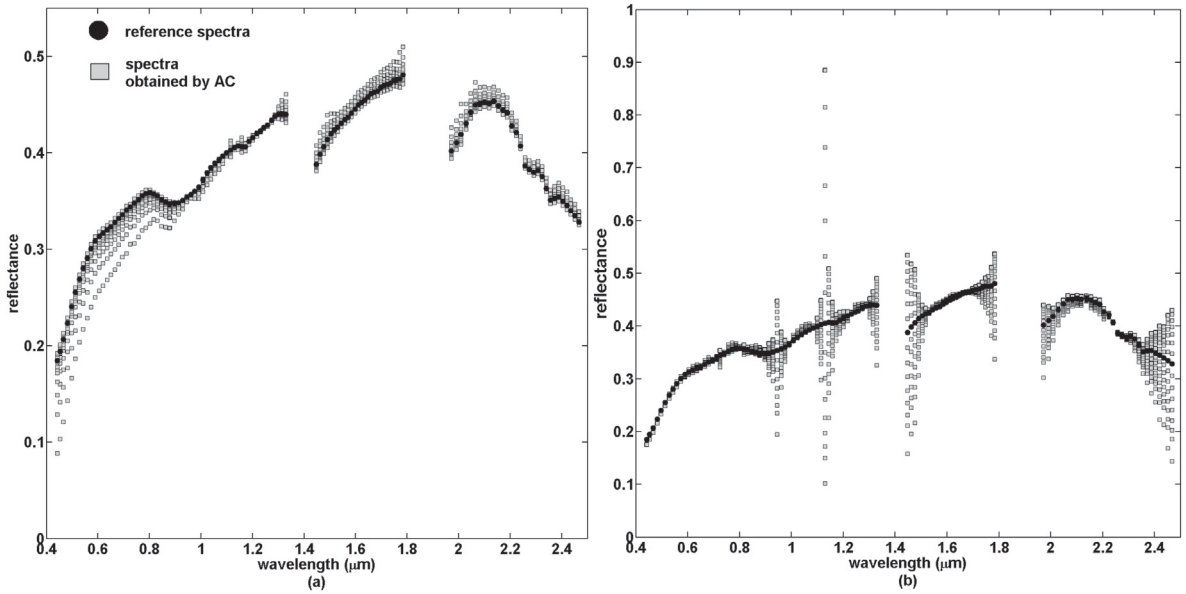

Fig. 13. Deviation in the spectral quality due to the uncertainty in visibility in (a) and CWV in (b). The visibility is varying between 6 and 26 km with a true visibility at 15 km and CWV is varying between 1.0 and 2.25 g·cm^{-2} with a true value at 1.5 g·cm^{-2}.

Table 4
Effect of dark and bright targets on the performance with true visibility conditions for reflectance estimates.

Albedo	Visibility (km)	Aerosol optical depth	SRE (dB)	NRMSE	MAPE (%)
Dark	60	0.14	64	$4.2e^{-04}$	$3.8e^{-02}$
Bright	60	0.14	72	$3.0e^{-04}$	$9.4e^{-03}$
Dark	15	0.47	52	$1.7e^{-03}$	$1.6e^{-01}$
Bright	15	0.47	58	$1.5e^{-03}$	$5.7e^{-02}$

noise level strongly influences the performance at both estimates in two ways: 1) the overall amplitude of the performance degrades as compared to the performances observed at 40 dB and 50 dB noise levels; 2) comparing the trend of the performances with the noiseless case, the distinct peak of the performances is not visible anymore i.e. the highest performance can be obtained around the true values of the parameters and not necessarily when the parameters are correctly set. These findings are more clearly visible for unmixing estimates.

For correlated noise with SNR of 40 and 50 dB, the decrease in the performances is smoother if column water vapor is overestimated as compared to if it is underestimated. Further, the distinct peak of the performances is also not achieved for 40 and 50 dB as compared to the noiseless case.

A comparison between the unmixing solutions reveals that FCLS-TV has superior performance than FCLS in noisy scenes. The superior performance of FCLS-TV is less important if noise decreases, confirming the previous results. This is valid for all combinations of atmospheric parameters. The optimal λ_{TV} values under various noisy conditions are given in Table 5.

6. Discussion and conclusions

This paper aimed to quantify the uncertainty propagation from

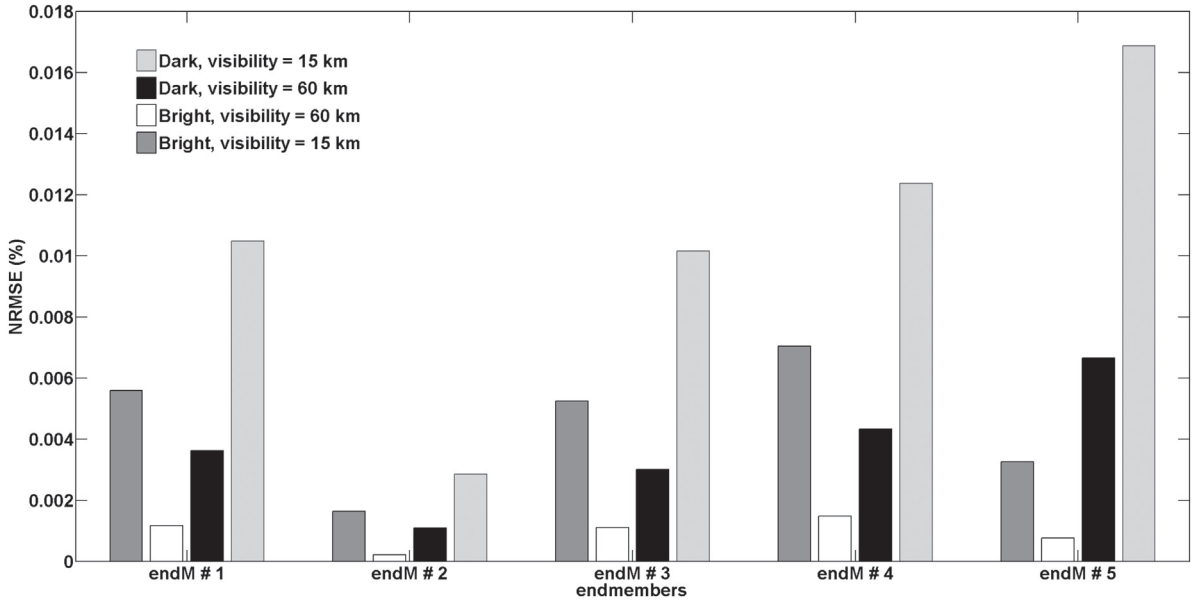

Fig. 14. The NRMSEs (%) obtained for the five endmembers quantify the effect of dark and bright targets with true visibility and column water vapor conditions for abundance estimates.

aerosol optical depth (AOD) and column water vapor to the fractional abundance estimates via reflectance estimates. It was applied to the HyMap hyperspectral sensor and there is no reason why it should also not be effective on other hyperspectral sensors. The method is simple to implement and can be extended to encompass other atmospheric trace gases and other atmospheric condition parameters.

One of the important contributions of this study is that the effect of uncertainty was analyzed and quantified. The results shown provide a useful insight into how a given uncertainty affects the performance at reflectance level and at subsequent applications (spectral unmixing). For instance, 30% degradation in performance (SRE) was observed under the high scattering conditions. This degradation came down to 6% under the moderate scattering conditions. The steepness in performance degradation significantly changes when the noise corrupts the data, especially under the high noise conditions. This indicates that the atmospheric settings, noise, and the parameter's deviation have a combined effect on the propagation of the uncertainty. Thus, an in-depth analysis of performance degradation due to the uncertainty in aerosol optical depth and column water vapor was performed for different atmospheric scenarios, covering low, moderate, and high scattering and absorption conditions for various noisy setups. The analysis identified performance degradation trends that were actually caused by the gradual shift in parameter values from their true value within the uncertainty limits (ranges) defined in the experiments.

We noted that the variability in aerosol optical depth influenced the amplitude of the retrieved spectra. Its influence was not linear, in the sense that deviations from the reference spectra depend upon the surface reflectance of the target, the wavelength, and the scattering conditions (Seidel et al., 2012). This observation is consistent with our previous work (Bhatia et al., 2015). For high aerosol optical depth values and high surface reflectance (> 0.3), the estimated reflectance was higher than the reference reflectance, whereas for low surface reflectance (< 0.3) estimated spectra were lower than reference spectra. This consistently happened for spectra of all considered endmembers. An opposite pattern was observed for low scattering conditions. In Fraser and Kaufman (1985), a threshold $P_c = \frac{\mathrm{AOD}}{\rho_t(\lambda)}$ was introduced as a critical parameter to determine how the estimated reflectance changes due to aerosol scattering. Applying this threshold we found that if $P_c > 1$, then the estimated surface reflectance was underestimated, otherwise it was overestimated. The changes in the estimated reflectance were negligible when aerosol optical depth approaches the reflectance value.

Variation in column water vapor influenced the retrieved spectra mainly in the bands around the atmospheric water vapor absorption features. Uncertainty in column water vapor affected the performance more severely than uncertainty in aerosol optical depth, because variation in column water vapor significantly distorted the spectral shape. This was evident from the low performance obtained for maximum

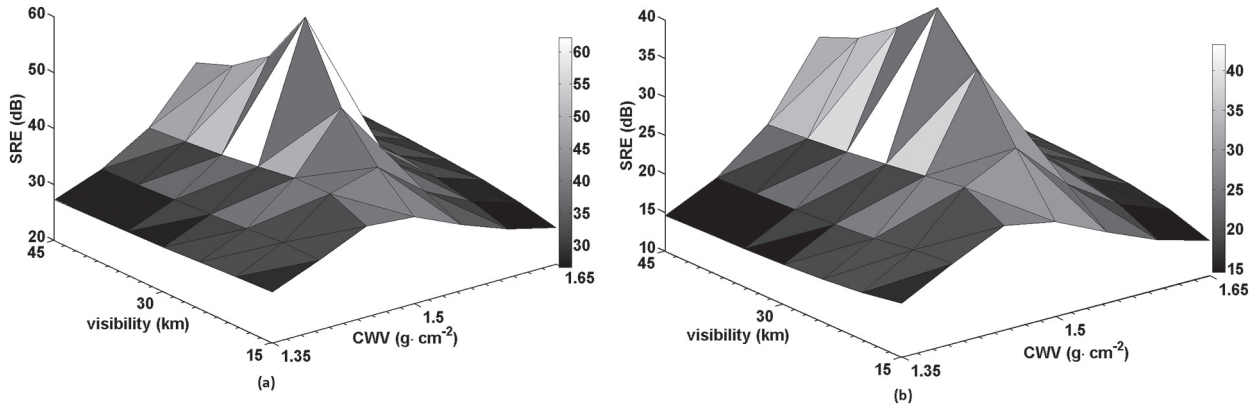

Fig. 15. SRE (dB) values for bivariate analysis of column water vapor and visibility for reflectance estimates (a) and abundance estimates (b) without correlated noise.

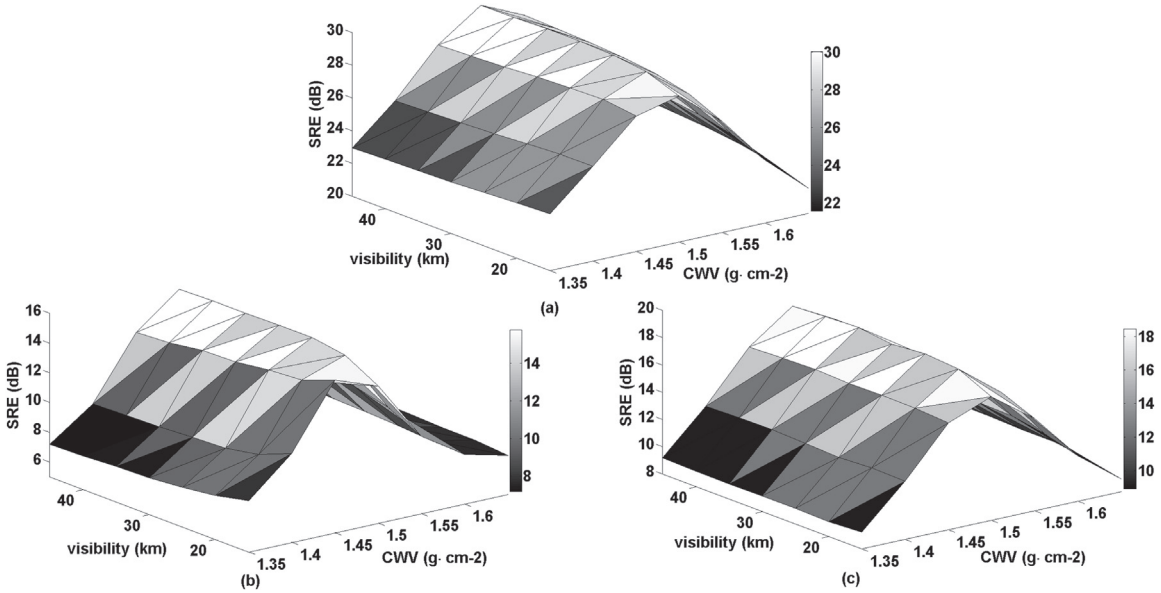

Fig. 16. SRE (dB) for the vegetation dataset with correlated noise (SNR = 30 dB) for reflectance estimate (a), for the abundance estimate with FCLS solution (b), and with FCLS-TV solution (c) for variations in column water vapor and visibility.

Table 5
Optimal λ_{TV} for different noise levels and for various combinations of column water vapor and visibility.

Noise level (dB)	Column water vapor (g·cm^{-2})	Visibility (km)	Optimal λ_{TV}
No-noise	1.35–1.65	15–45	0
30	1.35	15	0.03
30	1.40–1.65	20–45	0.01
40	1.35	15	0.03
40	1.40–1.65	20–45	0.01
50	1.35–1.45	15	0.01
50	1.50–1.65	20–45	0

deviation in aerosol optical depth as compared to maximum deviation in column water vapor. The uncertainty in aerosol optical depth, however, strongly influenced the quality of the abundance maps if the endmembers were spectrally similar, especially if high atmospheric scattering occurred.

Further, the performance of reflectance estimates was always higher than that of abundance estimates. This might be due to the inherent limitations of the unmixing method and their numerical approximations. Without noise FCLS and FCLS-TV are comparable because spatial homogeneity in the datasets introduces only negligible improvements of the fractional abundance values in noiseless scenes.

A difference in maximum attainable performance observed for high scattering conditions could be attributed to the presence of bright and dark targets in a scene. Bright targets reflect more radiation energy than dark targets. Thus, the majority of the at sensor radiance consists of photons that are not scattered. In contrast, most of the photons for the dark targets are scattered (Lindstrot et al., 2012). This contribution amplifies under high scattering conditions resulting in performance degradation. In this paper, we do not explicitly explore the effect of albedo on the parameters estimation. From our experience working with the real images in the CDPC, we found that surface albedo affects the parameters estimation by widening the parameters uncertainty. The surface albedo becomes a source of the parameters uncertainty. As an outlook of this work, a sensitivity analysis can be performed to apportion the contribution of sources of uncertainty to reflectance estimates.

Effective ranges of column water vapor and aerosol optical depth were within the 90% confidence interval from their true values. Thus, for the bivariate analysis, we varied visibility and column water vapor values within relatively narrow ranges: 15–45 km and 1.35–1.65 g·cm^{-2}, respectively. Outside this interval, the performance strongly degraded and saturated to a low value. Such effective ranges could be a useful measure for calibrating the value of the two parameters in optimizing the performance under uncertainty. Under high noise conditions (SNR = 30 dB), both spectral quality and unmixing performance are strongly degraded, whereas the effect of scattering becomes less important. A high noise level therefore has a weaker influence on the performance trend for column water vapor than for aerosol optical depth, resulting in a distinct peak of the performance. Thus, in the presence of high noise in airborne data, uncertainty in atmospheric correction parameters and data noise affect the final products jointly.

Because of the asymptotic decreasing relation between aerosol optical depth and visibility, care should be taken when using visibility as a substitute to aerosol optical depth, especially under high scattering conditions where aerosol optical depth is highly sensitive to visibility values (see Fig. 7). Ideally, estimation of aerosol optical depth can be obtained from the AErosol RObotic NETwork (AERONET) stations (Holben et al., 1998). However, most of the airborne campaigns and many satellite images do not include an AERONET site location. Alternatively, aerosol optical depth measurements can be taken from handheld instruments. This requires ground measurements at the time of satellite or airborne image acquisition, which is often hard to collect and is impossible to obtain for archived imagery. Two measures that are often used for visibility are horizontal extinction coefficients derived from the horizontal visibility measured at airport stations and image based methods. Horizontal based visibility estimation leads to inaccurate values because of the dependency of estimates to the viewing direction. Lower values of visibility are reported when looking in the direction of the sun due to the strong forward scattering radiation (Schlapfer, 1998). It results in errors in horizontal visibility that are significantly higher than those derived from image based methods and standard satellite products. Airborne campaigns are also normally not acquired under high scattering conditions. Therefore, errors seen at 0–10 km visibility in Wilson et al. (2015) are unlikely to be experienced with operational remote sensing.

The present study can be further extended to take other atmospheric correction parameters into account. Effects of adjacency can be investigated in scenes where heterogeneity and/or topographic effects are

important to include. It would be interesting to compare different unmixing methods while considering the reflectance uncertainty due to atmospheric condition parameters. Moreover, as uncertainties were also introduced by the applied unmixing method, a comparison between unmixing methods can be extended with inclusion of model uncertainty. Experiments with spectral libraries containing a large number of spectral signatures are recommended, as those were beyond the scope of the current study.

References

Baldridge, A.M., Hook, S.J., Grove, C.I., Rivera, G., 2009. The ASTER spectral library version 2.0. Remote Sens. Environ. 113, 711–715. http://dx.doi.org/10.1016/j.rse.2008.11.007.

Bateson, C.A., Asner, G.P., Wessman, C.A., 2000. Endmember bundles: a new approach to incorporating endmember variability into spectral mixture analysis. IEEE Trans. Geosci. Remote Sens. 38, 1083–1094. http://dx.doi.org/10.1109/36.841987.

Berk, A., Anderson, G.P., Acharya, P.K., Chetwynd, J.H., Bernstein, L.S., Shettle, E.P., Matthew, M.W., Adler-Golden, S.M., 2000. MODTRAN4 user's manual. In: Technical Report Air Force Research Laboratory, Hanscom AFB, MA, USA and Naval Research Laboratory, Washington, DC, USA and Spectral Sciences, Burlington, MA, USA.

Bhatia, N., Tolpekin, V.A., Reusen, I., Sterckx, S., Biesemans, J., Stein, A., 2015. Sensitivity of reflectance to water vapor and aerosol optical thickness. IEEE J. Sel. Top. Appl. Earth Obs. Remote Sens. 8, 3199–3208. http://dx.doi.org/10.1109/JSTARS.2015.2425954.

Biesemans, J., Sterckx, S., Knaeps, E., Vreys, K., Adriaensen, S., Hooyberghs, J., Meuleman, K., Kempeneers, P., Deronde, B., Everaerts, J., Schlapfer, D., Nieke, J., 2007. Image processing work flows for airborne remote sensing. In: Proceedings 5th EARSeL Workshop on Imaging Spectroscopy.

Bioucas-Dias, J.M., Plaza, A., Dobigeon, N., Parente, M., Du, Q., Gader, P., Chanussot, J., 2012. Hyperspectral unmixing overview: Geometrical, statistical, and sparse regression-based approaches. IEEE J. Sel. Top. Appl. Earth Obs. Remote Sens. 5, 354–379. http://dx.doi.org/10.1109/JSTARS.2012.2194696.

Carrere, V., Conel, J., 1993. Recovery of atmospheric water vapor total column abundance from imaging spectrometer data around 940 nm–sensitivity analysis and application to airborne visible/infrared imaging spectrometer(AVIRIS) data. Remote Sens. Environ. 44, 179–204. http://dx.doi.org/10.1016/0034-4257(93)90015-P.

Chambolle, A., 2004. An algorithm for total variation minimization and applications. J. Math. Imaging Vision 20, 89–97.

Cocks, T., Jenssen, T., Stewart, A., Wilson, I., Shields, T., 1998. The HyMap TM airborne hyperspectral sensor: The system, calibration and performance. In: Proceedings of the 1st EARSeL Workshop on Imaging Spectroscopy, Zurich, pp. 37–42.

Diner, J.D., Martonchik, V.J., Kahn, R.A., Pinty, B., Gobron, N., Nelson, D.L., Holben, B.N., 2005. Using angular and spectral shape similarity constraints to improve MISR aerosol and surface retrievals over land. Remote Sens. Environ. 94, 155–171.

ENVI-Team, 2014. ENVI classic tutorial: Vegetation hyperspectral analysis. In: Technical Report. Exelis Visual Information Solutions, Inc..

Fraser, R.S., Kaufman, Y.J., 1985. The relative importance of aerosol scattering and absorption in remote sensing. IEEE Trans. Geosci. Remote Sens. GE-23, 625–633.

Gao, B.C., Davis, C., Goetz, A., 2006. A review of atmospheric correction techniques for hyperspectral remote sensing of land surfaces and ocean color. In: 2006 IEEE International Symposium on Geoscience and Remote Sensing, pp. 1979–1981. http://dx.doi.org/10.1109/IGARSS.2006.512.

Gao, B.C., Montes, M.J., Davis, C.O., Goetz, F.H.A., 2009. Atmospheric correction algorithms for hyperspectral remote sensing data of land and ocean. Remote Sens. Environ. 113, S17–S24. http://dx.doi.org/10.1016/j.rse.2007.12.015.

Haan, J.F., Kokke, J.M.M., 1996. Remote sensing algorithm development Toolkit I: Operationalization of atmospheric correction methods for tidal and inland waters. In: Development Toolkit NRSP-2 96-16 Netherlands Remote Sensing Board.

Heinz, D.C., Chang, C.I., 2001. Fully constrained least squares linear spectral mixture analysis method for material quantification in hyperspectral imagery. IEEE Trans. Geosci. Remote Sens. 39, 529–545.

Holben, B.N., Eck, T.F., Slutsker, I., Tanré, D., Buis, J.P., Setzer, A., Vermote, E., Reagan, J.A., Kaufman, Y.J., Nakajima, T., Lavenu, F., Jankowiak, I., Smirnov, A., 1998. AERONET–A federated instrument network and data archive for aerosol characterization. Remote Sens. Environ. 66, 1–16. http://dx.doi.org/10.1016/S0034-4257(98)00031-5.

Iordache, M.D., Bioucas-Dias, J.M., Plaza, A., 2011. Sparse unmixing of hyperspectral data. IEEE Trans. Geosci. Remote Sens. 49, 2014–2039.

Iordache, M.D., Bioucas-Dias, J.M., Plaza, A., 2012. Total variation spatial regularization for sparse hyperspectral unmixing. IEEE Trans. Geosci. Remote Sens. 50, 484–4502. http://dx.doi.org/10.1109/TGRS.2012.2191590.

Jonathan, E., Bertsekas, D.P., 1992. On the Douglas—Rachford splitting method and the proximal point algorithm for maximal monotone operators. Math. Program. 55, 293–318. http://dx.doi.org/10.1007/BF01581204.

Keshava, N., 2003. A survey of spectral unmixing algorithms. Lincoln Lab. J. 14, 55–78.

Kokaly, R.F., Clark, R.N., Swayze, G.A., Livo, K.E., Hoefen, T.M., Pearson, N.C., 2017. USGS spectral library version 7. In: Technical Report. U.S. Geological Survey Data Series 1035 (61 pp.).

Lenoble, J., 1998. Atmopsheric Radiative Transfer. A. Deepak Publishing, Virginia.

Lindstrot, R., Preusker, R., Diedrich, H., Doppler, L., Bennartz, R., Fischer, J., 2012. 1D-Var retrieval of daytime total columnar water vapour from MERIS measurements. Atmos. Meas. Tech. 5, 631–646.

Matlab-Toolbox, 2012. Hyperspectral imagery synthesis (EIAs) toolbox. In: Technical Report Grupo de Inteligencia Computacional, Universidad del País Vasco / Euskal Herriko Unibertsitatea (UPV/EHU), Spain. The MathWorks, Inc., Massachusetts, United States.

Qu, Z., Kindel, B.C., Goetz, A.F.H., 2003. The high accuracy atmospheric correction for hyperspectral data (HATCH) model. IEEE Trans. Geosci. Remote Sens. 41, 1223–1231. http://dx.doi.org/10.1109/TGRS.2003.813125.

Remer, L.A., Kaufman, Y.J., Tanre, D., Mattoo, S., Chu, D.A., Martins, J.V., Li, R.R., Ichoku, C., Levy, R.C., Kleidman, R.G., Eck, T.F., Vermote, E., Holben, B.N., 2005. The MODIS aerosol algorithm, products, and validation. J. Atmos. Sci. 62, 947–973.

Richter, R., 2007). Atmospheric/Topographic correction for airborne imagery (ATCOR-4 user guide). In: User Guide. DLR-German Aerospace Center.

Richter, R., Schlapfer, D., Muller, A., 2006. An automatic atmospheric correction algorithm for visible/NIR imagery. Int. J. Remote Sens. 27, 2077–2085.

Rodger, A., 2011. SODA: A new method of in-scene atmospheric water vapor estimation and post-flight spectral recalibration for hyperspectral sensors: Application to the HyMap sensor at two locations. Remote Sens. Environ. 115, 536–547. http://dx.doi.org/10.1016/j.rse.2010.09.022.

Schlapfer, D., 1998. Differential Absorption Methodology for Imaging Spectroscopy of Atmospheric Water Vapor (Ph.D. thesis). Remote Sensing Laboratories, Department of Geography Universiy of Zurich.

Seidel, F.C., Kokhanovsky, A.A., Schaepman, M.E., 2012. Fast retrieval of aerosol optical depth and its sensitivity to surface albedo using remote sensing data. Atmos. Res. 116, 22–32. http://www.sciencedirect.com/science/article/pii/S0169809511000718.

Stamnes, K., Tsay, S.C., Wiscombe, W., Jayaweera, K., 1988. Numerically stable algorithm for discrete-ordinate-method radiative transfer in multiple scattering and emitting layered media. Appl. Opt. 27, 2502–2509. http://dx.doi.org/10.1364/AO.27.002502.

Sterckx, S., Vreys, K., Biesemans, J., Iordache, M.D., Bertels, L., Meuleman, K., 2016. Atmospheric correction of APEX hyperspectral data. Misc. Geogr. Reg. Stud. Dev. 20.

Verhoef, W., Bach, H., 2003. Simulation of hyperspectral and directional radiance images using coupled biophysical and atmospheric radiative transfer models. Remote Sens. Environ. 87, 23–41.

Wilson, R.T., Milton, R.J., Nield, J.M., 2015. Are visibility-derived AOT estimates suitable for parameterizing satellite data atmospheric correction algorithms? Int. J. Remote Sens. 36, 1675–1688.